colorants

MDPI

Article

Mathematical Approach to Optimizing the Panchromatic Absorption of Natural Dye Combinations for Dye-Sensitized Solar Cells

Noah B. Manz * and Paul A. Fuierer *

Materials and Metallurgical Engineering Department, New Mexico Institute of Mining and Technology, 801 Leroy Pl, Socorro, NM 87801, USA

* Correspondence: nmanzf35@gmail.com (N.B.M.); paul.fuierer@nmt.edu (P.A.F.)

Abstract: The goal of this work was to optimize the combination of natural dyes producing panchromatic absorption matched to the AM1.5 solar spectrum for use in dye sensitized solar cells (DSSCs). Six classes of dyes (Anthocyanins, Betalins, Chlorophyll, Xanthonoids, Curcuminoids and Phycobilins) were explored. UV-Vis data and radial basis function interpolation were used to model the absorbance of 2568 combinations, and three objective functions determined the most commensurable spectrum. TiO_2 anodes were sensitized with 42 dye combinations and IV measurements made on simple cells. The absorbance-optimized combination yielded an efficiency of only 0.41%, compared to 1.31% for a simple 1:1 molar ratio of Curcuminoids and α-Mangostin, which showed symbiotic effects. Our results indicate that panchromatic absorption alone is not sufficient to predict optimal DSSC performance, although the mathematical approach may have broader application.

Keywords: dye-sensitized solar cells; natural dyes; panchromatic absorption; radial basis function interpolation

Citation: Manz, N.B.; Fuierer, P.A. Mathematical Approach to Optimizing the Panchromatic Absorption of Natural Dye Combinations for Dye-Sensitized Solar Cells. *Colorants* **2023**, *2*, 90–110. https://doi.org/10.3390/colorants2010007

Academic Editors: Nadia Barbero, Carlotta Pontremoli and Simone Galliano

Received: 24 January 2023
Revised: 21 February 2023
Accepted: 1 March 2023
Published: 2 March 2023

1. Introduction

Dye-sensitized solar cells (DSSCs) are a promising class of thin film photovoltaics due to their competitive cost/power ratio, high manufacturability and performance in low and artificial light conditions [1]. They were first developed in the 1970s but have seen steady growth and improvements resulting in higher output performance, thanks in no small part to the development of the eponymous Grätzel cell in 1988 [2]. These cells are functionally distinct from the more familiar p–n junction solar cells and rely on light absorption from a photosensitive dye molecule adsorbed to the surface of a wide bandgap semiconductor (usually TiO_2). In contrast to a p–n junction cell, where the exciton generation and charge carrier separation both occur in the same material (within the depletion region), the DSSC separates these functions between the dye and the semiconducting anode respectively [3]. Excited electrons are first generated in the dye molecule and then transferred into the conduction band of the anode by virtue of the difference in energy levels between the two states (reference Figure 1). Global charge carrier separation then occurs as the electron is transferred into a transparent conducing oxide (TCO) layer. These high energy electrons can be used to do work before ultimately being injected into a cathode material (usually Pt) which catalyzes the reduction of an electrolyte redox couple (e.g., I^-/I_3^-) [3]. Diffusion of these ion species within the electrolyte solvent then reduces the original oxidized dye molecule, allowing the cycle to begin again.

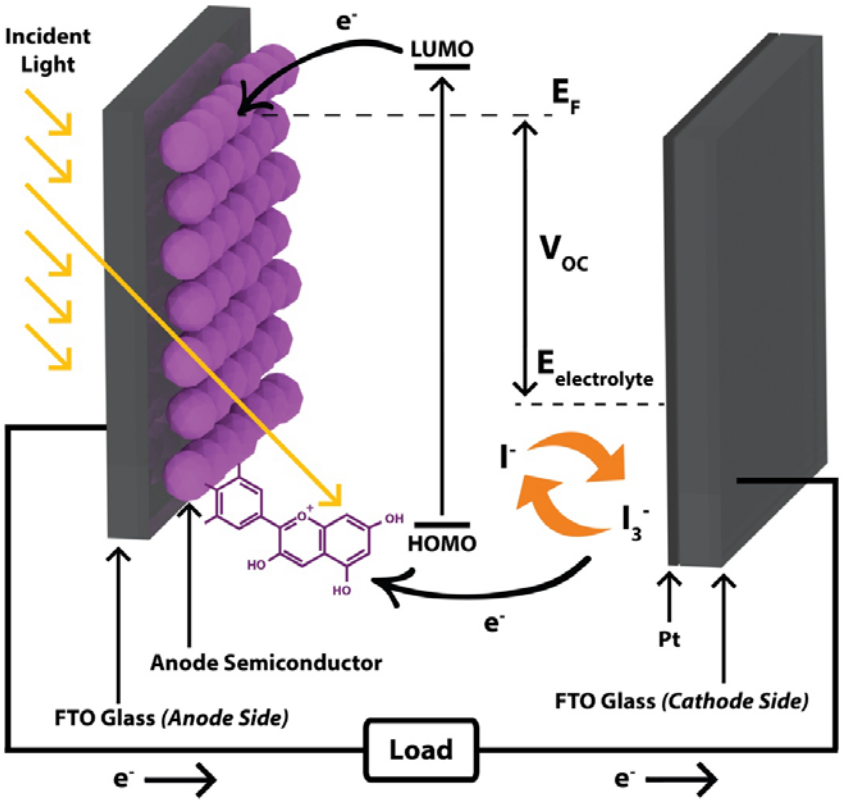

Figure 1. Schematic diagram of a dye-sensitized solar cell (DSSC) showing the major components and positions of relevant energy levels.

Due to the many components of a DSSC, much research has been generated exploring ways to improve and optimize each part. With regards to the photosensitive dye molecules, synthetic Ruthenium-containing complexes have been produced and yield the current record-holding DSSC efficiency of 14.1% by EPFL (achieved in mid-2013) [1]. While this efficiency record is impressive, one remaining problem concerns the price of these Ruthenium complexes. In fact, current commercial prices are nearing USD 1700/g (Sigma Aldrich, SKU: 791245), which undermines the DSSC value proposition of low cost/power ratios. This has given rise to another salient topic in DSSC literature: attempting to use natural plant-based dyes in lieu of the much more expensive synthetic alternatives. There has been a tremendous amount of research on the subject with a specific focus on the topic of co-sensitization of multiple dyes to increase and widen the absorption characteristics of the device (yielding so-called panchromatic absorbance) [4]. This co-sensitization is known to result in increased DSSC efficiency, though the magnitudes reported in the literature vary greatly based on the constituent dyes as well as the combination ratios. In general, efficiency increases between 30% and 120% are reported [5–18].

Given the potential of natural dye co-sensitization, it is surprising that no papers have made an attempt to quantitatively optimize dye combinations to maximize DSSC efficiency. This might be partially due to the ambiguity of "optimization" given the numerous criteria DSSC dyes must satisfy for proper functioning including the prevalence of anode-anchoring moieties, peak absorption wavelength, redox potential and the positions of the HOMO and LUMO energies [1]. While a model which considers all of these factors would be ideal, the gap this paper explores as a starting point is absorbance-optimized dye combinations, and specifically assesses the degree to which the light-harvesting efficiency (*LHE*) profiles of different dye combinations match the AM1.5G solar irradiance spectrum. It was hypothesized that DSSCs co-sensitized with a panchromatic dye solution, which is optimized for the AM1.5G solar irradiance spectrum, will result in the highest overall efficiency due to the broadband spectral absorbance of the device.

2. Materials and Methods

2.1. Dye Preparation

The six individual dyes used in this work (Figures 2 and 3) were extracted from the precursors indicated in Table 1. For convenience, each dye has also been assigned a one-letter abbreviation. Detailed information about extraction methods can be found in the linked Supplementary Materials as well as in [19]. These dyes were selected due to their high absorbance in the visible spectrum as well as their appropriate chemical/electrochemical properties, including anode-anchoring moieties, HOMO/LUMO level placement and formal redox potential, which are listed in Table A1. The concentrations of the extracts are also presented in Table 1 and were necessary in order to generate the equimolar combinations of constituent dyes as described in the following paragraph.

Figure 2. Final bulk dye solutions. From left to right: Phycobilin, Chlorophyll, α-Mangostin, Curcuminoids, Anthocyanin, Betalin. Note that while the extracts are purported to be single-chemical species in Table 1, they are actually combinations of multiple substituted variants of the parent molecule of the dye class.

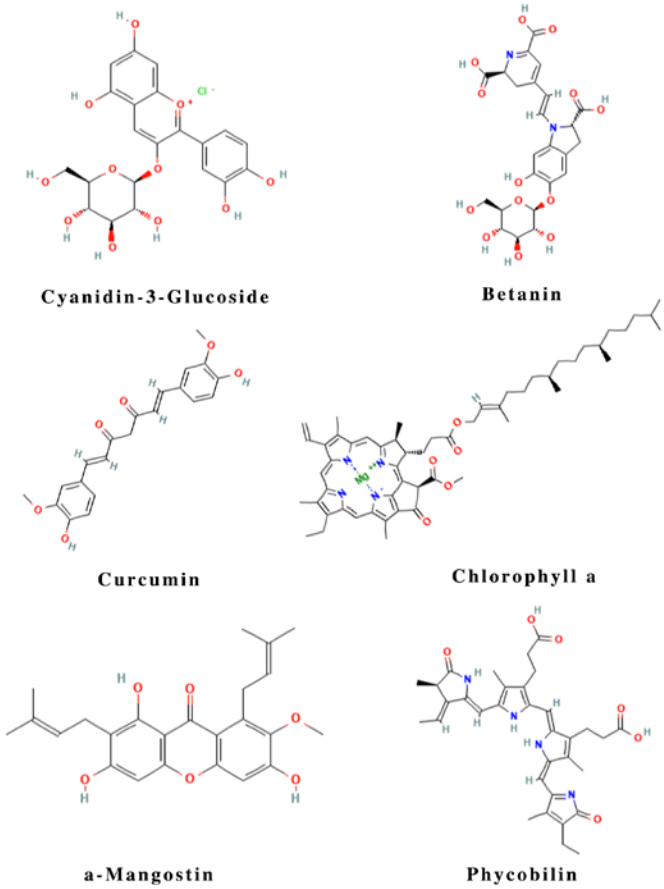

Figure 3. Structures of the major chemical species indicated in Table 1 [30–35]. Note the presence of appropriate oxygen-containing functional groups for anode binding, also shown in Table A1.

Table 1. Dye classes showing organic precursor materials, major chemical species and the measured concentration of dye extracts via the Beer–Lambert relation. The molar extinction coefficients of the major chemical species were selected from the literature as a proxy for the larger dye class.

Dye Class (*One Letter Abbreviation*)	**Major Chemical Species**	**Precursor Material**	**Molar Extinction Coefficient (M^{-1} cm^{-1})**	**Dye Concentration (μM)**
Anthocyanins (*A*)	Cyanidin-3-Glucoside [20]	Fresh frozen Aroniaberries	34,300 @ 520 nm [21]	0.74
Betalins (*B*)	Betanin [22]	Fresh frozen Prickly Pear	65,000 @ 535 nm [22]	0.03
Curcuminoids (*K*)	Curcumin [23]	Turmeric powder	55,000 @ 425 nm [24]	1.88
Chlorophyll (*C*)	Chlorophyll a,b [25]	Dried Spinach	70,000 @ 430 nm [26]	0.12
Xanthonoids (*M*)	α-Mangostin [27]	Mangosteen Pericarp dietary supplements	51,800 @ 425 nm [28]	0.14
Phycobilins (*P*)	Phycobilin [29]	Blue Spirulina platensis powder	98,000 @ 620 nm [29]	0.02

After determining the concentrations of the constituent dye extracts, UV-Vis absorption spectra were collected for a total of 42 unique, equimolar dye combinations. Specifically, this included every 1:1 molar combination of two dyes (C(6,2) = 15 total), every 1:1:1 molar combination of three dyes (C(6,3) = 20 total) and for the equimolar combination of all six dyes. For reference, a 1:1 molar combination of dyes X and Y is denoted XY (1:1:1 of X, Y, Z is XYZ). For a complete list of all dye combinations generated, as well as for a photo of each combination, refer to the Supplementary Materials. In addition, transparent TiO_2 anodes were produced (using Solaronix Ti-Nanoxide T/SP paste) and sensitized with these same 42 combinations. UV-Vis absorbance data was then collected for these "anode adsorbed" dyes which were blanked against an unsensitized TiO_2 anode.

2.2. Radial Basis Function Interpolation and LHE Optimization

The 42 dye combinations introduced in Section 2.1 represent a baseline for the combinations explored in this work and were not the only combinations analyzed. However, analysis of the remaining combinations (2568 total) was achieved using a mathematical method to quantitatively optimize the ratio of constituent dyes. Specifically, this was achieved by first generating radial basis function interpolations of all UV-Vis data from the 42 combinations at a particular wavelength. In other words, generating a surface in R^7 with precession through all the measured absorbance data at, for example, 400 nm. By repeating this interpolation for every wavelength in the domain [340, 800 nm], a set of interpolation functions was generated which could then individually be evaluated at a specific input combination which yielded the final absorbance profile for that input. Despite the apparent complexity, one advantage of this method is the ability to continually update the model with real-world data beyond just the 42 individual data points used in this work. For a deeper intuition about this statement, as well as for an explanation of the problem with a simple rule of mixtures, refer to the animations of Figures A1–A3 provided in Appendix A. Finally, once the absorbance profile was calculated for an arbitrary dye combination, it could be converted to *LHE* and compared to the AM1.5G solar irradiance spectrum in order to determine the degree of commensurability. In this work, three objective functions (so-called "fitment conditions") were proposed to perform this comparison. These fitment conditions (which were all intended to be maximized) were the Pearson correlation and the covariance between the absorbance curve as well as the AM1.5G solar irradiance spectrum and the definite integral of the absorbance curve. By repeating this process for all possible dye combinations and searching for the one which yielded the greatest commensurability

via the fitment conditions, it was possible to calculate an optimized dye combination which could then be evaluated in an actual DSSC.

More formally, the RBF interpolation began by defining data matrix d which contained the absorbance values for all dye combinations over the entire wavelength domain and matrix v which contained the volume fractions of each dye in each combination. An example data matrix is shown in Equation (1), where n = 42 corresponding to the 42 combinations of Section 2.1 and w = 461 corresponding to 461 wavelength data points between 340 and 800 nm. In the example of the v matrix, $x = [V_{1,1}, V_{2,1}, -V_{6,1}]^{\mathrm{T}}$ would be the combination of constituent dyes leading to the absorbance data of $y = [A_{1,1}, A_{2,1}, -A_{\mathrm{w},1}]^{\mathrm{T}}$.

$$d = \begin{bmatrix} A_{1,1} & A_{1,2} & \cdots & A_{1,n} \\ A_{2,1} & A_{2,2} & \cdots & A_{2,n} \\ \vdots & \vdots & \ddots & \vdots \\ A_{w,1} & A_{w,2} & \cdots & A_{w,n} \end{bmatrix} \tag{1}$$

$$v = \begin{bmatrix} V_{1,1} & V_{1,2} & \cdots & V_{1,n} \\ V_{2,1} & V_{2,2} & \cdots & V_{2,n} \\ \vdots & \vdots & \ddots & \vdots \\ V_{6,1} & V_{6,2} & \cdots & V_{6,n} \end{bmatrix} \tag{2}$$

Then, for a particular wavelength, $\lambda \in [1, w]$, an interpolation function was generated which maps every column in **v** to the corresponding absorbance data in the row $[\mathrm{A}_{\lambda,1}, \mathrm{A}_{\lambda,2}\text{–}\mathrm{A}_{\lambda,n}] \in d$. To achieve this, a set of radially symmetric basis function translates, ψ, were first constructed and which are centered (in R^7) at point $x_i = (V_{1,i}, V_{2,i}\text{–}V_{6,i})$ for $i \in [1, n]$. Due to the symmetric nature of these basis functions, this can be easily done by passing the L2 norm, r, as an argument [36]. The particular basis function used in this work was the inverse multiquadric shown in Equation (4).

$$r_i = ||X - x_i||_2 \tag{3}$$

$$\psi(r_i) = \psi(||X - x_i||_2) = \frac{1}{\sqrt{1 + (\varepsilon r_i)^2}} \tag{4}$$

Here, X is any input vector which spans R^6 with an L1 norm equal to one. This vector represents the independent variable, which is passed into the interpolation function to obtain the resulting ordinate value. The interpolation function s(X) is then defined to be the weighted sum of the individual basis function translates, as shown in Equation (5).

$$s(X) = \sum_{i=1}^{n} \beta_i \psi(||X - x_i||_2) \tag{5}$$

The appropriate weights, β, were then obtained by solving the following linear system [35]. The vector f represents the data being interpolated (i.e., $[A_{\lambda,1}, A_{\lambda,2}\text{–}A_{\lambda,n}]^{\mathrm{T}}$).

$$A\beta = f \tag{6}$$

$$A = \begin{bmatrix} \psi_1(||X - x_1||_2) & \psi_1(||X - x_2||_2) & \cdots & \psi_1(||X - x_n||_2) \\ \psi_2(||X - x_1||_2) & \psi_2(||X - x_2||_2) & \cdots & \psi_2(||X - x_n||_2) \\ \vdots & \vdots & \ddots & \vdots \\ \psi_n(||X - x_1||_2) & \psi_n(||X - x_2||_2) & \cdots & \psi_n(||X - x_n||_2) \end{bmatrix} \tag{7}$$

$$A^{-1}A\beta = A^{-1}f \quad iff \quad \det(A) \neq 0 \tag{8}$$

$$\beta = A^{-1}f \tag{9}$$

By repeating this process for every wavelength $\lambda \in [1, w]$, a set of 461 interpolation functions was generated which could be individually evaluated for the arbitrary input vector X to return the resulting absorbance spectrum. These absorbance values were then then converted to an *LHE* spectrum ($LHE = 1 - 10^{-A}$) [37]. Since absorbance is measured on a log scale, this conversion was performed to normalize the spectrum between 0 and 1. Then, each of the three fitment conditions was applied to solve for the commensurability, α between *LHE* and the AM1.5G solar irradiance spectrum, φ. This spectrum, φ, like the *LHE* spectrum, was also normalized between 0 and 1. The three fitment conditions are shown in Equations (10)–(12).

$$\alpha_{corr} = \frac{cov(\varphi,\ LHE)}{\sigma_{\varphi}\sigma_{LHE}} \tag{10}$$

$$\alpha_{int} = \int_{340}^{800} LHE d\lambda \tag{11}$$

$$\alpha_{cov} = cov(\varphi,\ LHE) \tag{12}$$

For each fitment condition, the dye combination which yielded the greatest commensurability, α, was determined to be the optimized dye combination for that condition. In the remainder of this work, the combinations satisfying all three fitment conditions are reported since each condition implies different assumptions about the meaning of "maximum commensurability" between an *LHE* spectrum and AM1.5G. For example, in some cases, the correlation between the two datasets might be high (see Figure 4, line C) even though the overall integral value is low. In reality, a more optimal *LHE* profile might exhibit slightly lower correlation, but at the same time a much greater overall integral value (see Figure 4, line D). The purpose of the different fitment conditions in Equations (10)–(12) was to account for such ambiguity by analyzing the spectra for these different attributes. A visual animation showing how different transformations on a dataset affect these fitment conditions is provided in Appendix A as Figure A4.

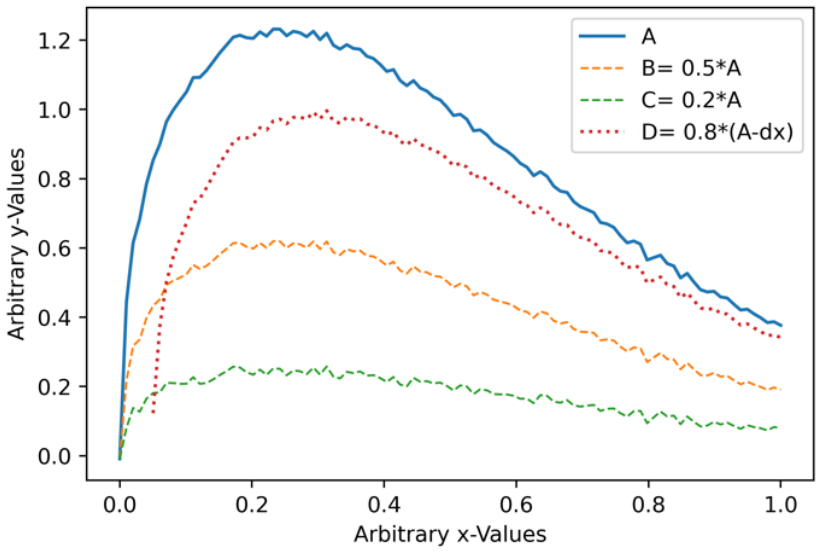

Figure 4. Visualization of the importance of the different fitment conditions. Dataset A is a proxy for the solar irradiance spectrum, and three transformations of this dataset are shown as proxies for an *LHE* spectrum (i.e., B, C and D). Dataset D is likely the optimal *LHE* spectrum in this case, but due to the small rightward shift, will exhibit a lower correlation than either datasets B or C. The three fitment conditions in Equations (10)–(12) are intended to account for such scenarios.

This mathematical approach to matching spectral data is also suggested to have broader applications in situations where it is either infeasible to directly simulate a resulting spectrum, or it is impractical to collect the required quantity of data to analyze all

combinations outright. Additionally, this method provides a framework for the consideration of factors whose influence are not obvious without a first-principles approach. In this work for example, the dependence of dye absorbance on factors such as pH or solvent composition could also have been considered. Such factors are challenging to account for otherwise, and this ability to quantify their influence in a relatively straightforward way is suggested to be one of the useful characteristics of this spectral matching approach.

3. Results and Discussion

3.1. UV-Vis Absorbance Measurements

The UV-Vis spectra collected for the six individual dyes is displayed in Figure 5 and shows relatively high broadband absorbance in the visible spectrum. Phycobilins and α-Mangostin appeared to exhibit the greatest overall peak absorbance at ~400 nm for the bulk solution UV-Vis measurements. The results of the anode-adsorbed UV-Vis measurements are shown in Figure 6. All data reported in this work (including plots) are available for public access in Mendeley Data, doi: 10.17632/d9f44dspd5.3, reference [38].

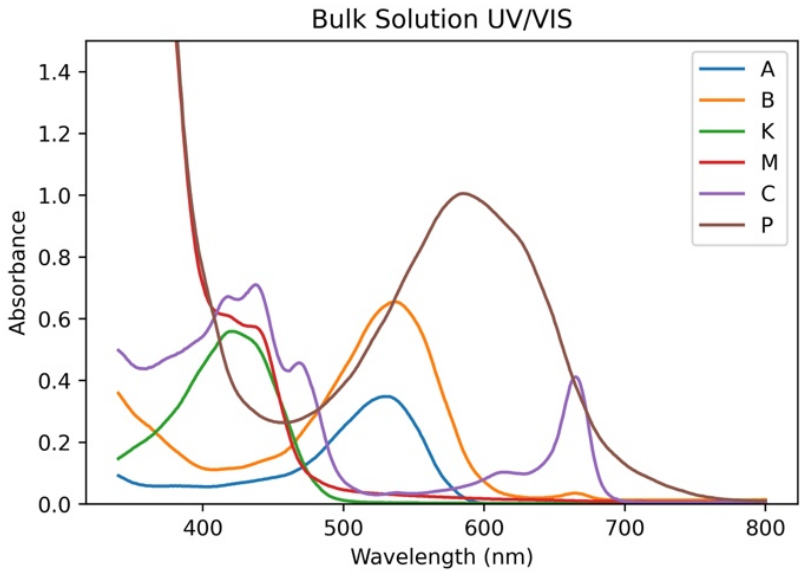

Figure 5. UV-Vis spectra of the six constituent dyes (10 μM concentration).

In the anode-adsorbed spectra, both Curcuminoids and α-Mangostin exhibited high peak absorbance values in the low wavelength regime and Betalin exhibited high absorbance across the spectrum. Chlorophyll and Phycobilin, on the other hand, exhibited relatively low absorbance and perhaps a blue shift and peak quenching, respectively, when compared to solution absorbance. This suggests significant differences in aggregation and binding affinity to the TiO_2 anode between dye families. These differences stem from differences in the molecular structure and anchoring moieties (see Figure 3 and Table A1). For example, recent work with cyanine dye structural variants (each with carboxylic acid-anchoring moieties) reveals unique dye binding configurations on a TiO_2 substrate, resulting in different optical absorbance cross sections, *LHE* and HOMO-LUMO distributions [39]. Furthermore, significant self-anti-aggregation capacity has been reported for dyes containing two or more anode-anchoring moieties [40]. The low binding affinity of Chlorophyll in particular may also be explained by the severely sterically hindered carbonyls on the tetrapyrrole ring which exacerbate aggregation effects.

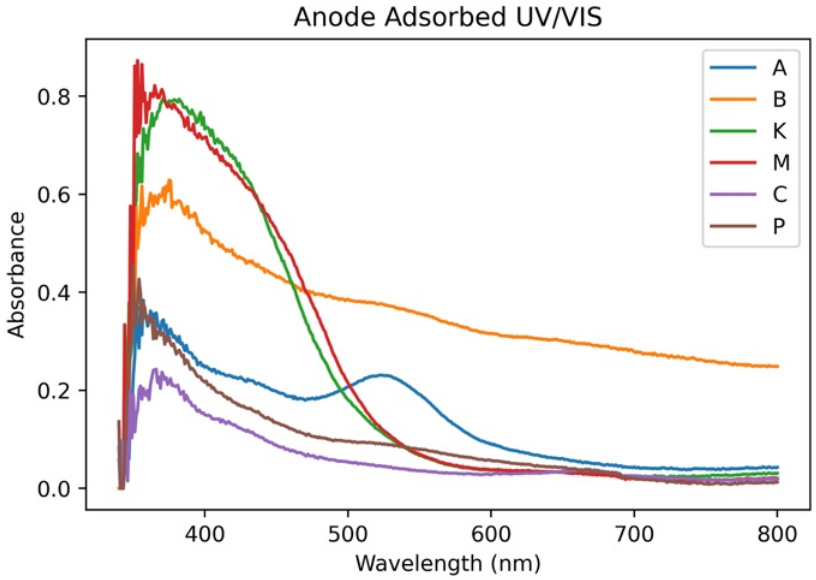

Figure 6. UV-Vis spectra of the six constituent dyes adsorbed to transparent TiO_2 anodes (Solaronix T/SP paste).

UV-Vis data was also collected for the 42 combinations outlined in Section 2.1, and the results showing peak absorbance values and the absorbance integral for both the bulk solution and anode-adsorbed datasets are shown in Table 2. The cells colored orange indicate global minima for the respective value while the green-colored cells indicate global maxima. Plots of these spectra are provided in the Supplementary Materials.

Table 2. Results of the bulk solution and anode-adsorbed UV-Vis analysis for all 42 dye combinations. Note that absorbance and the absorbance integral are unitless values.

Combination	Bulk Solution Peak Absorbance	Bulk Solution Integral	Anode-Adsorbed Peak Absorbance	Anode-Adsorbed Integral
A	0.35	**34.69**	0.38	65.15
B	0.66	81.84	0.63	**165.01**
K	0.56	49.90	0.80	101.53
M	3.64	168.94	0.87	104.31
C	0.71	98.17	**0.24**	28.98
P	2.46	286.43	0.45	43.84
AB	0.49	63.15	0.45	66.22
AK	0.81	100.41	0.37	61.87
AM	3.41	170.20	0.67	123.40
AC	0.69	102.19	0.27	40.16
AP	2.57	293.47	0.33	46.38
BK	0.54	52.71	0.29	42.44
BM	3.39	208.88	0.68	69.36
BC	0.89	165.36	0.44	82.99
BP	2.46	308.67	0.37	**26.29**
KM	2.36	128.56	**1.06**	122.38
KC	1.20	145.31	0.41	43.00

Table 2. *Cont.*

Combination	Bulk Solution Peak Absorbance	Bulk Solution Integral	Anode-Adsorbed Peak Absorbance	Anode-Adsorbed Integral
KP	2.41	318.23	0.47	62.28
MC	3.74	235.69	0.91	102.10
MP	3.50	285.53	0.66	60.28
CP	2.45	301.86	0.51	59.30
ABK	0.50	70.19	0.45	51.18
ABM	**3.84**	232.12	0.47	57.55
ABC	0.83	157.65	0.58	62.85
ABP	**0.32**	41.38	0.25	40.08
AKM	3.81	217.62	0.64	92.77
AKC	1.14	146.07	0.46	55.76
AKP	2.45	300.71	0.59	99.61
AMC	3.67	230.30	0.57	100.88
AMP	3.40	286.19	0.44	51.72
ACP	2.43	323.68	0.28	42.68
BKM	3.38	248.50	0.52	67.45
BKC	0.69	111.51	0.46	36.96
BKP	2.44	331.19	0.51	51.07
BMC	3.00	267.46	0.36	44.26
BMP	3.01	266.14	0.32	32.19
BCP	2.40	**341.48**	0.40	43.52
KMC	3.54	263.29	0.83	90.33
KMP	2.76	241.07	0.49	97.11
KCP	1.27	200.71	0.36	36.05
MCP	2.69	257.95	0.63	49.99
ABKMCP	2.55	251.09	0.82	85.43
Average	**2.13**	**199.68**	**0.52**	**66.83**

These data show that the greatest bulk solution and the anode-adsorbed peak absorbance came from the ABM and KM combinations, respectively. Furthermore, BCP was shown to exhibit the largest absorbance integral for the bulk solution data while pure Betalin extract exhibited the greatest integral for the anode-adsorbed dyes. The combinations A, C, BP and ABP exhibited the lowest values in the respective categories. These initial results reaffirm that dyes exhibiting high anode-adsorbed absorbance characteristics (e.g., B, KM, MC, AM, etc.) are particularly well suited as DSSC dyes due to their high binding affinity TiO_2.

3.2. Radial Basis Function Interpolation and LHE Optimization Results

The results of the mathematical modelling from Section 2.2 are presented in Tables 3 and 4 showing the results for bulk solution and anode-adsorbed UV-Vis data, respectively (in terms of volume fractions of equimolar constituents). These are the dye combinations which satisfy the fitment conditions in Equations (10)–(12). The AM1.5G solar irradiance data were obtained from the National Renewable Energy Laboratory (NREL) and the resolution (or minimum step size) of the volume fractions was 0.1 [41]. This yielded a total of 2568 unique combinations for analysis. Interestingly, it was observed that both the correlation and covariance fitments yielded the same results, which is believed to be a consequence of the relatively consistent standard deviations of the calculated *LHE*

spectra, along with the somewhat coarse volume fraction resolution. Therefore, despite being mathematically distinct, these two fitment conditions converged to the same global maximum (i.e., the same optimized dye combination). This could be addressed in the future by using a finer volume fraction resolution (e.g., 0.01).

Table 3. Optimized dye solutions from solution UV-Vis data (reference Figure 7, quadrants I and II).

Combination	Fitment Condition	V_A	V_B	V_K	V_M	V_C	V_P
1	Correlation	0.4	0.4	0	0	0	0.2
2	Integral	0.3	0	0	0	0.3	0.4
3	Covariance	0.4	0.4	0	0	0	0.2

Table 4. Optimized dye solutions from anode-adsorbed UV-Vis data (reference Figure 7, quadrants III and IV).

Combination	Fitment Condition	V_A	V_B	V_K	V_M	V_C	V_P
4	Correlation	0	0	0.3	0.3	0	0.4
5	Integral	0	1.0	0	0	0	0
6	Covariance	0	0	0.3	0.3	0	0.4

The *LHE* plots for all six optimized combinations are shown in Figure 7 and referenced against AM1.5G. In the case of the optimized combinations from the bulk solution UV-Vis data, the value of the three fitment conditions becomes obvious since combinations one and three (the correlation and covariance fitment conditions, respectively) show high commensurability with the peak value of the solar irradiance spectrum, as expected. However, the breadth of the plot is fairly low, suggesting that the overall absorption capacity might be limited. In contrast, the integral fitment condition does not exhibit quite as high peak-to-peak absorbance commensurability, but instead shows a very broad *LHE* spectrum with a high overall integral value. These six optimized dye combinations were then used to sensitize DSSCs in Section 3.3.

3.3. IV Measurements

DSSCs were manufactured for each dye combination from Section 2.1, plus the six optimized combinations from Section 3.2. The IV data collected for each of these DSSCs is compiled in Table 5. Measurements were collected with an input power of 36 mW (0.36 cm^2 × 100 mW/cm^2) using an AM1.5G filter. A UV blocker was not used.

From these results, it was found that the single best performing dye was α-Mangostin (M), with an efficiency of 1.00%. The best 1:1 combination was KM, with an efficiency of 1.31% (reference Figure 8), and the best 1:1:1 combination was KMC, with an efficiency of 0.84%. The 1:1:1:1:1:1 combination of all six dyes yielded an efficiency of only 0.18%, clearly suggesting that more constituent dyes does not equate to higher DSSC performance. This is likely due to dye aggregation, which is known to quench molecular excited states and can significantly hinder electron injection efficiencies [42]. The average efficiency for all 42 combinations was 0.29%, with a standard deviation of 0.25%, which highlights how well the KM combination in particular performed. Finally, dye combinations one and three, corresponding to the maximum correlation/covariance fitment of the bulk solution UV-Vis data, yielded an efficiency of just 0.18%, while the bulk solution integral fitment (combination two) resulted in an efficiency of 0.11%. Alternatively, results from the anode-adsorbed UV-Vis data were more encouraging, with combinations four and six (correlation/covariance fitment) yielding an efficiency of 0.41%, which outperformed the

statistical average of the original 42 combinations by a factor of almost 1.5 (see Figure 9). However, combination five corresponding to the anode-adsorbed integral fitment only yielded an efficiency of 0.22%, suggesting that, in this case, the higher peak-to-peak commensurability of the covariance-optimized *LHE* spectra outperformed the high integral value *LHE* (see Figure 7, quadrants III and IV).

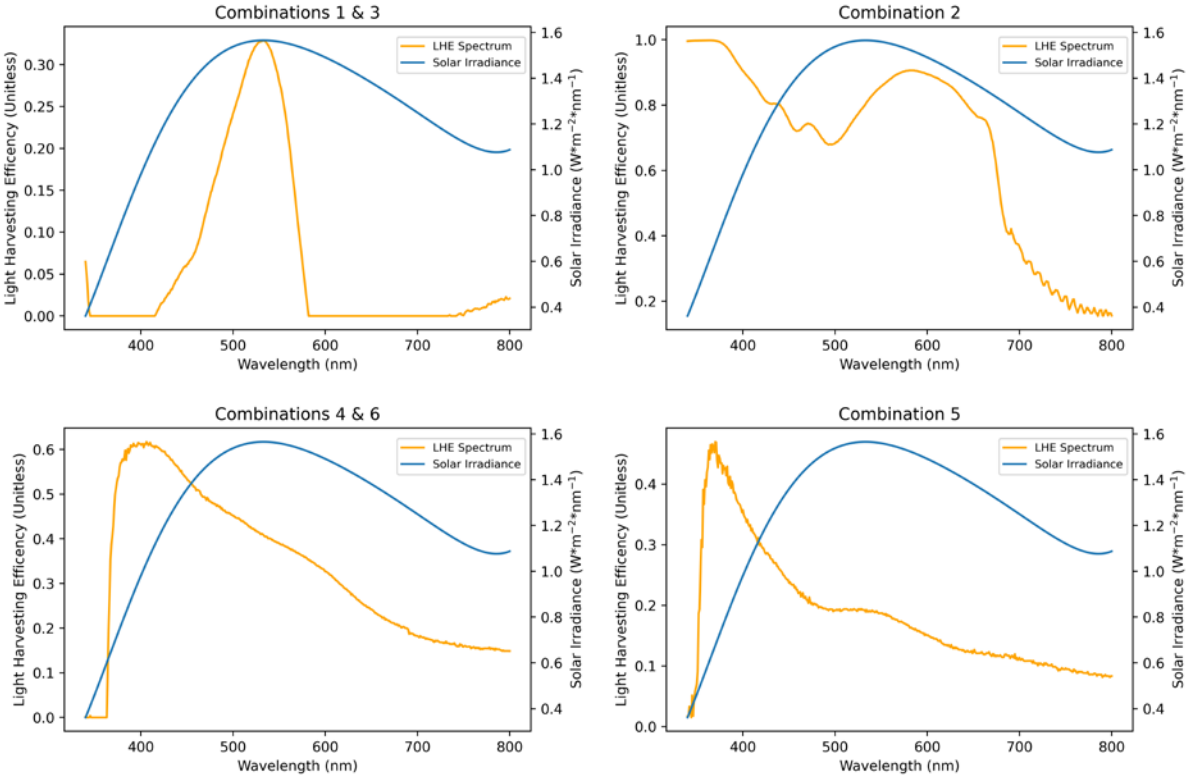

Figure 7. *LHE* of the six optimized combinations referenced against the AM1.5G solar irradiance spectrum. Note the parity of combinations 1 and 3 as well as combinations 4 and 6 as indicated in Tables 3 and 4.

Table 5. IV data of all DSSCs produced in this work.

Combination	J_{sc} (mA/cm^2)	V_{oc} (V)	FF (Unitless)	Efficiency (%)
A	0.442	0.482	0.517	0.110
B	0.775	0.574	0.489	0.217
K	0.822	0.553	0.522	0.237
M	2.642	0.620	0.612	1.003
C	0.447	0.225	0.284	0.028
P	**0.214**	0.523	0.660	0.073
AB	0.856	0.607	0.684	0.354
AK	1.042	0.499	0.528	0.275
AM	1.514	0.536	0.584	0.474
AC	0.506	0.502	0.557	0.141
AP	0.389	**0.145**	0.268	**0.015**
BK	0.825	0.617	0.686	0.349
BM	0.714	0.612	0.410	0.178
BC	1.247	0.632	0.691	0.544
BP	0.322	0.576	0.629	0.116
KM	**3.039**	0.461	0.672	**1.308**

Table 5. *Cont.*

Combination	J_{sc} (mA/cm^2)	V_{oc} (V)	FF (Unitless)	Efficiency (%)
KC	1.206	0.592	0.570	0.406
KP	0.417	0.538	0.647	0.145
MC	1.214	0.290	0.333	0.117
MP	1.325	0.562	0.394	0.293
CP	0.492	0.464	**0.227**	0.052
ABK	0.822	0.572	0.702	0.330
ABM	0.750	0.609	0.460	0.210
ABC	0.914	0.638	**0.755**	0.440
ABP	0.583	0.608	0.595	0.247
AKM	1.614	0.345	0.295	0.164
AKC	0.900	0.529	0.520	0.248
AKP	0.239	0.421	0.464	0.046
AMC	1.433	0.529	0.409	0.310
AMP	0.675	0.557	0.487	0.183
ACP	0.447	0.546	0.412	0.100
BKM	1.125	**0.668**	0.647	0.486
BKC	0.331	0.598	0.586	0.115
BKP	0.731	0.582	0.706	0.300
BMC	1.081	0.665	0.696	0.492
BMP	0.989	0.604	0.687	0.410
BCP	0.489	0.582	0.700	0.199
KMC	1.883	0.640	0.695	0.837
KMP	0.456	0.495	0.498	0.112
KCP	0.472	0.537	0.579	0.147
MCP	0.992	0.573	0.588	0.334
ABKMCP	0.564	0.605	0.534	0.182
Combinations 1 and 3	0.567	0.555	0.585	0.184
Combination 2	0.497	0.483	0.457	0.109
Combinations 4 and 6	1.075	0.636	0.601	0.410
Combination 5	0.775	0.574	0.489	0.217
Average	**0.888**	**0.538**	**0.546**	**0.288**

Interestingly, none of the lowest-performing dye combinations from Table 5 agreed with the lowest value predictions from Table 2, which shows that absorbance profiles alone are not sufficient to determine an optimal dye combination. However, it does appear that a general positive trend is observed between peak anode absorbance and DSSC efficiency, despite a few exceptions. In order to better understand the effects of co-sensitization on each individual class of dye molecule, Figure 10 was developed, which shows the IV performance of the individual dye (so-called "parent dye") against two separate bands. The solid orange line represents the average IV performance of all 1:1 dye combinations that contained the parent dye, and the dotted orange lines which generate the bands represent +/− one standard deviation away from that average. The green band is constructed in the same manner, except it considers all 1:1:1 combinations containing the parent dye. The black line is the untouched IV curve of the parent dye.

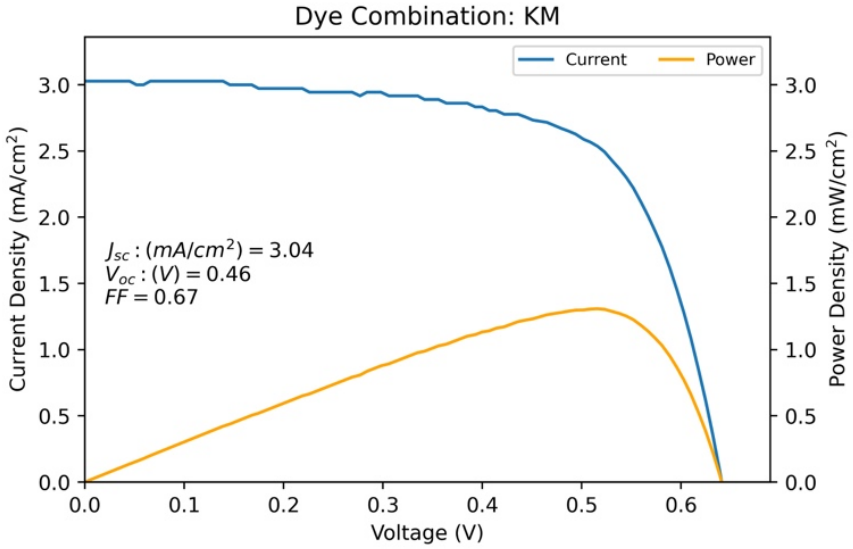

Figure 8. 1:1 molar Curcuminoids and α-Mangostin (KM) combination, with an efficiency of 1.31%.

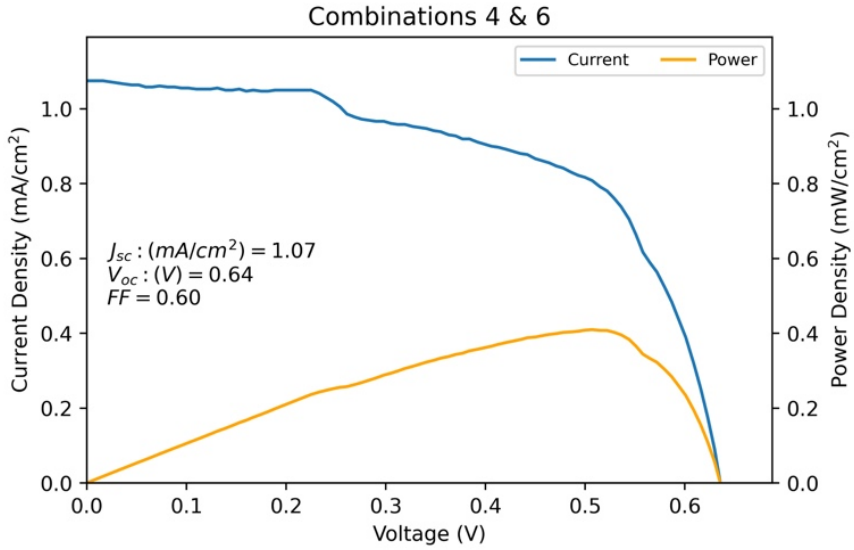

Figure 9. Optimized combinations 4 and 6, with an efficiency of 0.41%.

From these plots it can be seen that, in general, positive co-sensitization results are obtained from Anthocyanins, Curcuminoids, Chlorophyll and Phycocyanin, while Betalins showed only a marginal increase in the fill factor on average. Only the α-Mangostin dye appeared to be negatively affected by co-sensitization, which can be interpreted in one of two ways. Firstly, it may suggest that dye quenching or other interactions are occurring, or secondly, that the co-sensitization of high performing dyes such as α-Mangostin results in the dilution of the parent dye, which causes a decrease in IV performance due to the subsequent decrease in the surface concentration of the dye on the TiO_2 anode. This same logic can be applied to dyes such as Chlorophyll and Phycobilin, which suggests that the efficiency increase associated with co-sensitization of these dyes is due more to the addition of higher-performing single dyes rather than a true symbiotic process.

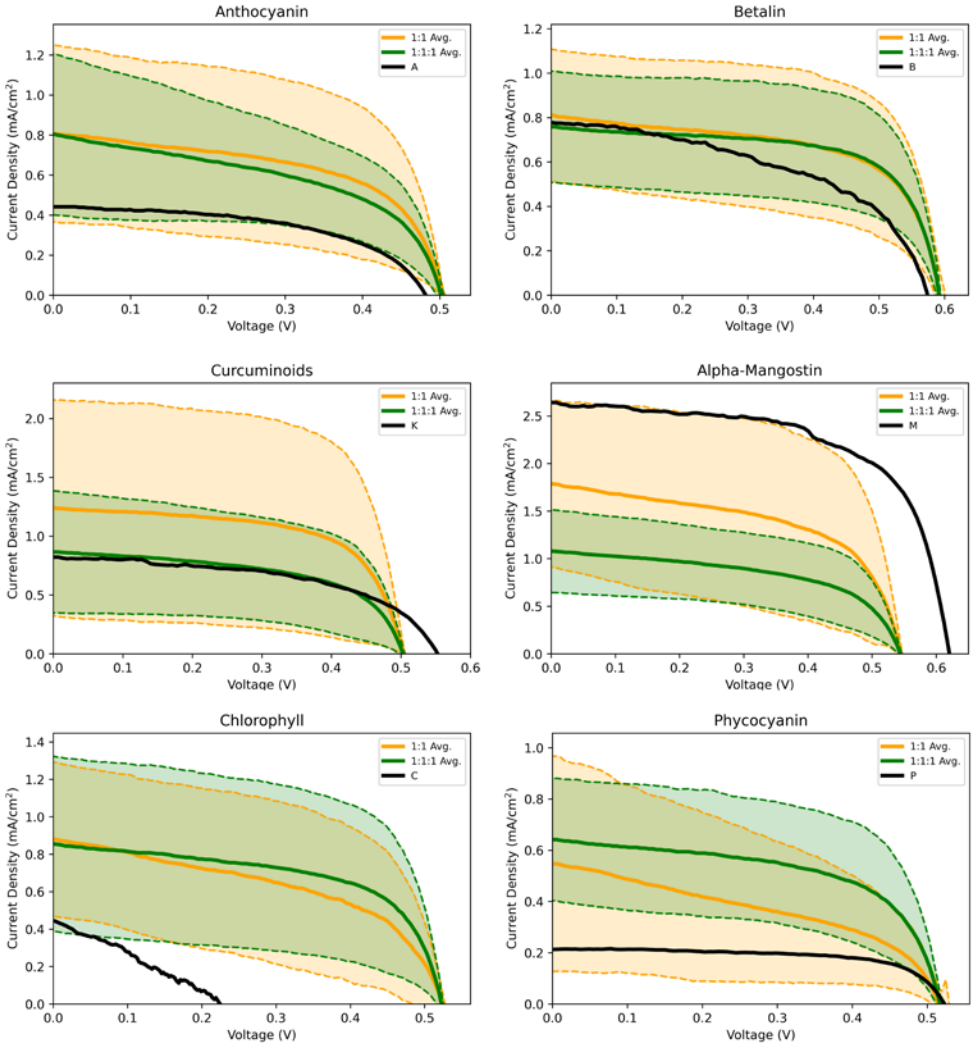

Figure 10. Co-sensitization trends of each parent dye. For example, the Anthocyanin plot shows an orange band averaged from the IV performance of: AB, AK, AM, AC and AP, and a green band averaged from the performance of: ABK, ABM, ABC, ABP, AKM, AKC, AKP, AMC, AMP and ACP.

3.4. Co-Adsorption of KM with 1:1 CDCA

Chenodeoxycholic acid (CDCA) is a naturally occurring bile acid which has been successfully used as a co-adsorbent in DSSC applications to increase cell efficiency. This is generally thought to be a result of the inhibition of recombination losses between the electrolyte and the anode which can occur when the passivation of the dye on the TiO_2 layer is incomplete [43]. Organic acids are also known to reduce dye aggregation, which increases electron injection efficiency and cell performance [40]. In the literature, CDCA co-adsorption has consistently reported efficiency gains between 20% and 60%, and it was attempted in this work to further improve the performance of the KM combination [44]. To achieve this, CDCA was simply dissolved in the KM dye combination in a molar ratio of 1:1. TiO_2 anodes were then sensitized normally. The IV results of this KM + 1:1 CDCA DSSC are shown in Figure 11.

The CDCA co-adsorbed KM dye combination yielded the highest efficiency reported in this work at 1.54%, though it is interesting to note the substantial decrease in the fill factor attributed to the higher series impedance from the CDCA adsorption. However, this was offset by the large overall increase in J_{sc}, leading to an 18% increase in efficiency for the KM + CDCA combination compared to the KM dye shown in Figure 8. This further demonstrates the impact of dye aggregation effects as noted in Section 3.1.

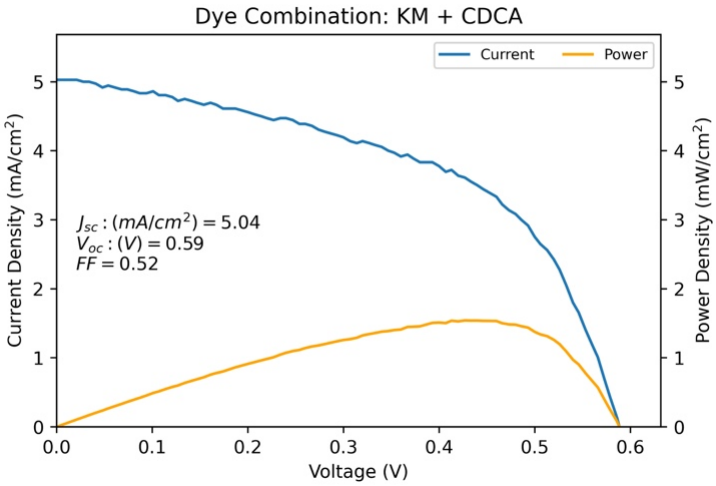

Figure 11. KM co-adsorbed with 1:1 CDCA.

3.5. UV Stability of KM Dye

A 10 mL sample of KM dye was placed in a UV crosslinking oven and irradiated at 254 nm for three consecutive 10-min intervals to analyze the dye's photostability. Absorption spectra were collected at the end of each 10-min period. These results are shown in Figure 12.

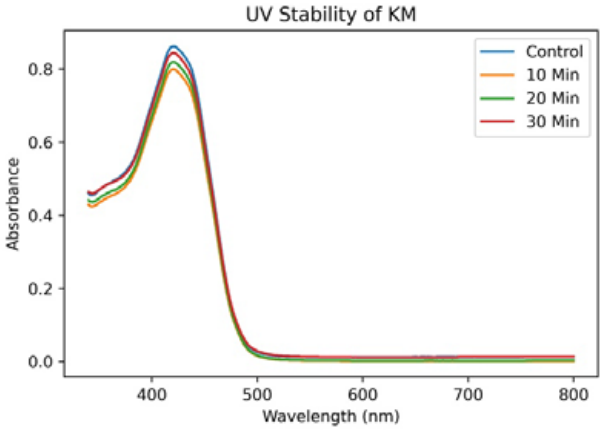

Figure 12. Photostability of KM dye after different durations of 254 nm UV exposure.

Even after 30 min, no significant UV-induced degradation appears to have occurred. Since the photostability of natural DSSC dyes has been observed to be a limiting characteristic in previous work (especially for dyes containing Anthocyanins [1,13]), the relative stability of the KM combination further highlights its promise as a natural DSSC sensitizer.

4. Conclusions

Co-sensitization of 42 DSSCs with unique combinations of six natural dyes (Anthocyanins (A), Betalins (B), Chlorophyll (C), α-Mangostin (M), Curcuminoids (K) and Phycobilins (P)) was performed in this work. Co-sensitization did, in general, result in higher IV performance, which is in accordance with the previous literature [5–18]. This symbiotic effect was observed in most 1:1 binary combinations. The highest-performing overall combination was KM, with an efficiency of 1.31%, and the efficiency of dye combinations appeared to decrease with the addition of further constituents. The best performing 1:1:1 combination was KMC, with an efficiency of 0.84%, and the 1:1:1:1:1:1 combination of all six dyes yielded an efficiency of only 0.18%. This is likely due to dye aggregation effects resulting in lower electron injection efficiencies [42]. The average efficiency for all 42 combinations was 0.29%, with a standard deviation of 0.25%, further highlighting the outlier nature of the KM and KMC combinations. The current study suggests that the KM

combination deserves further attention due to the performance in terms of both IV output and UV stability.

UV-Vis data from the 42 dye combinations was used to construct an interpolation function which then estimated the *LHE* profiles for a total of 2568 unique combinations. Three different fitment conditions were applied comparing these *LHE* spectra to the AM1.5G solar irradiance spectrum to obtain the absorbance-optimized dye combinations. DSSCs sensitized with these optimized combinations were then constructed, and the IV behavior was compared to that of the initial 42 combinations. The optimized dye combination one and three, corresponding to the covariance/correlation fitment of the bulk solution UV-Vis data, yielded an efficiency of 0.18%, while combination two (integral fitment) resulted in an efficiency of just 0.11%. Results from the anode-adsorbed UV-Vis data were more encouraging, with combination four and six (correlation/covariance fitment) yielding an efficiency of 0.41%, which outperformed the statistical average of the original 42 combinations. Combination five, however, corresponding to the anode-adsorbed integral fitment, only yielded an efficiency of 0.22%. From these results, it was determined that the anode-adsorbed UV-Vis data (peak absorbance values in specific) was a more reliable indicator of DSSC performance than the liquid solution UV-Vis data due to the absorbance shifts associated with dye binding. Therefore, it is suggested that future work also use anode-adsorbed data in-lieu of liquid solution UV-Vis data when analyzing dyes for DSSC applications.

This study provides further evidence that absorption profiles and panchromaticity alone are not sufficient to predict optimal DSSC performance, since KM yielded the highest efficiency in this work. KM was not explicitly predicted in Section 3.2 and was not shown to satisfy any of the fitment conditions, which is in contravention to the hypothesis. Additional factors such as electrochemical properties, excited state lifetime and MO-quenching mechanisms are clearly responsible for the observed differences between optimized absorbance and IV performance. Since it is known that electron transfer and relaxation processes are key to DSSC performance [1,3], ultra-fast spectroscopy (fluorescence) experiments might offer insight about the discrepancy. Such data might also be used in the combinatorial method presented herein to achieve predictive success. While the electron transfer complexities may limit the utility of the method for DSSCs, this mathematical optimization may serve useful in applications solely interested in absorbance and color matching using alternative dyes.

Supplementary Materials: DSSC fabrication and collection of IV data can be downloaded at: https://www.mdpi.com/article/10.3390/colorants2010007/s1, including dye extraction procedures, generation of dye combinations. References [45,46] are accessed in Supplementary Materials.

Author Contributions: Conceptualization, N.B.M.; data curation, N.B.M.; formal analysis, N.B.M.; funding acquisition, P.A.F.; investigation, N.B.M.; methodology, N.B.M.; project administration, N.B.M.; resources, P.A.F.; software, N.B.M.; supervision, P.A.F.; validation, P.A.F.; visualization, N.B.M.; writing—original draft, N.B.M.; writing—review and editing, P.A.F. All authors have read and agreed to the published version of the manuscript.

Funding: This research was funded, in part, by a research gift donation to the Department of Materials & Metallurgical Engineering at the New Mexico Institute of Mining and Technology.

Data Availability Statement: All data collected from this work have been made publicly available on Mendeley Data, doi: 10.17632/d9f44dspd5.3.

Acknowledgments: The authors would like to extend thanks to Emma Brudos and Annika Bauman from the New Mexico Tech Department of Materials and Metallurgical Engineering for their significant role in data collection, dye prep and DSSC manufacture, and without whom this project would not have been possible. Thanks are also extended to Praveen Patidar for assistance in establishing the dye extraction protocols, and to Nikolai Kalugin for assistance collecting UV-Vis data. Finally, thanks are extended to Julius Manz for assistance conceptualizing the optimization methods in Section 2.2 and for proofreading this manuscript.

Conflicts of Interest: The authors declare no conflict of interest.

Appendix A

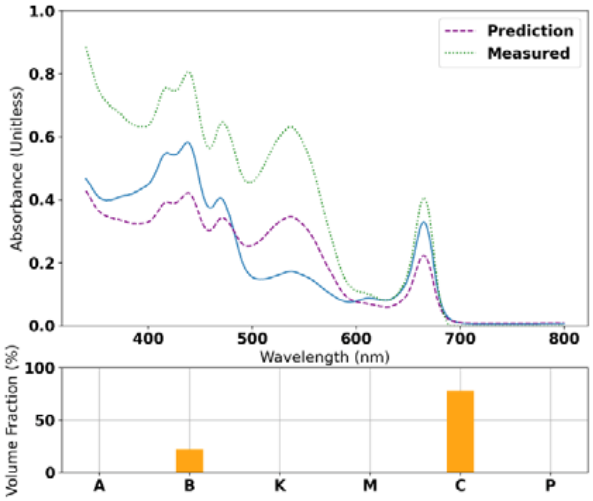

Figure A1. A linear rule of mixtures is applied to predict the absorbance profile (the blue curve) of a dye combination containing Betalin (B) and Chlorophyll (C). Notice that this profile exactly matches the data shown in Figure 5 for volume fractions of 100% Betalin and 100% Chlorophyll. The purple curve shows the predicted absorbance profile value for 50% Betalin and 50% Chlorophyll while the green curve shows the empirically measured profile for this same combination. The incommensurability of these two curves indicates that, while simple, a linear rule of mixtures is not adequate to accurately predict the absorbance profiles of unique dye combinations.

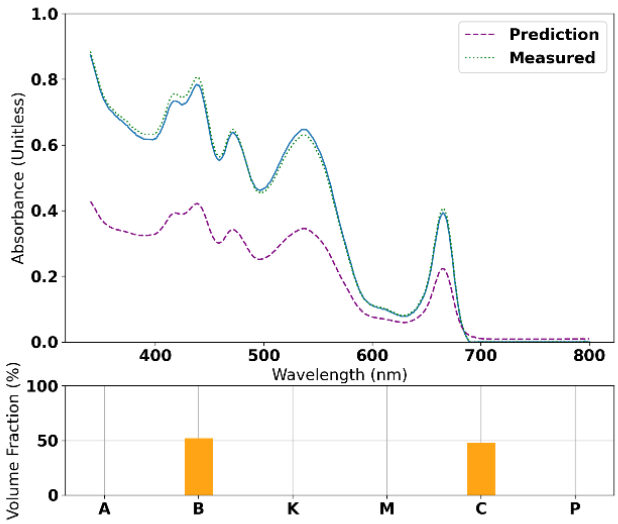

Figure A2. In contrast to the rule of mixtures shown in Figure A1, Figure A2 shows the radial basis function interpolation approach to modeling the absorbance profile of dye mixtures. Notice how the blue curve proceeds through the empirical 50/50 Betalin/Chlorophyll data while retaining the same 100% Betalin and 100% Chlorophyll profile starting points. Note: the purple curve represents the predicted absorbance for the rule of mixtures, not the RBF prediction. This purple curve is only intended to show how the RBF method succeeds where the rule of mixtures approach failed.

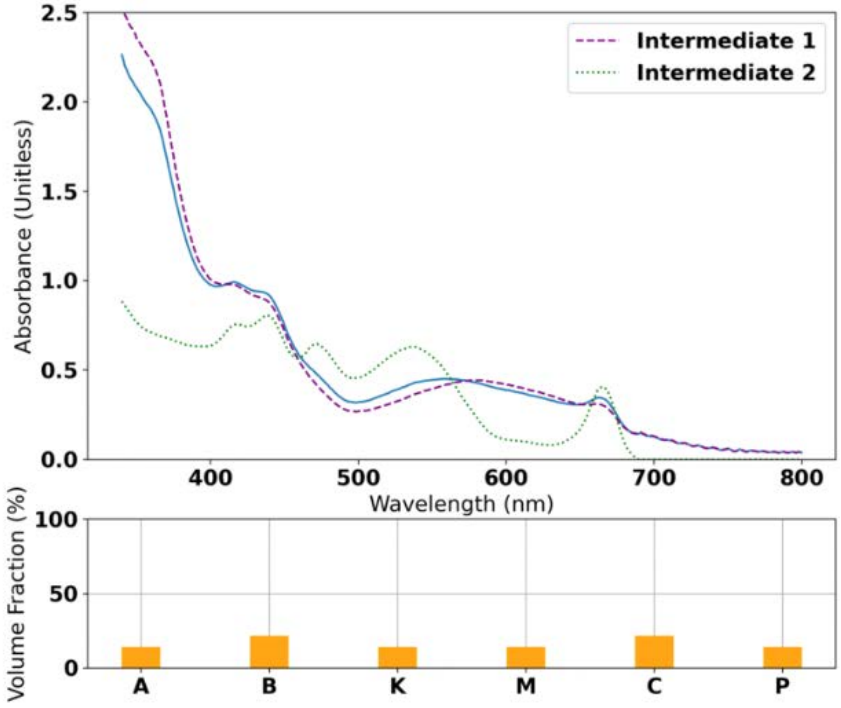

Figure A3. In addition to the 50/50 Betalin/Chlorophyll profile, the RBF interpolation scheme can be forced to proceed through an arbitrary number of data points. For example, in Figure A3, the predicted absorbance profile has been forced to fit the empirical UV-Vis data for the ABKMCP combination as well. This highlights one major advantage of the RBF method, which is that the model's error can be lowered to an arbitrary small degree simply by collecting and including more empirical data in the data matrix of Equation (1).

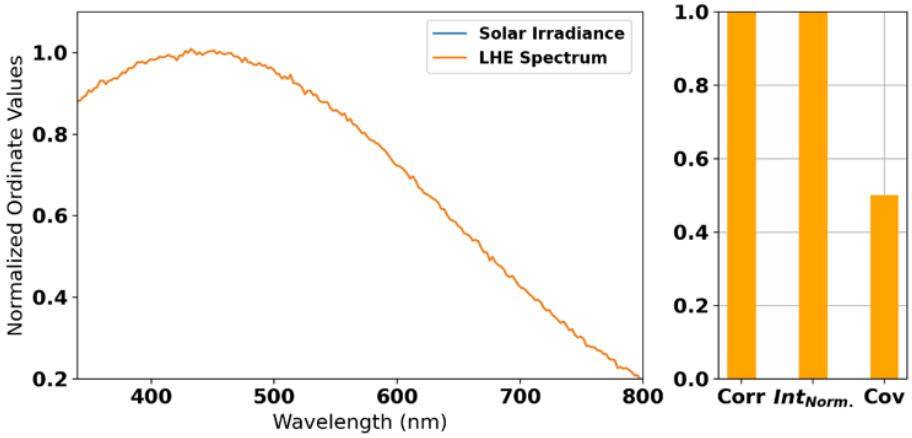

Figure A4. Proxies are shown for the AM1.5G solar irradiance spectrum and an *LHE* spectrum, along with the values of the correlation, integral (normalized to one) and covariance fitment conditions. Note how scaled (but not shifted) versions of the dataset affect the integral value but not the Pearson correlation. The ambiguity of "fitting" the *LHE* spectrum suggests that both these measures of peak-to-peak commensurability and high area-under-the-curve should be considered, which is the advantage of the covariance fitment condition.

Table A1. Miscellaneous dye information including the prevalent anode anchoring moiety, HOMO/LUMO levels referenced against vacuum level and the formal redox potential using a standard Ag/AgCl electrode).

Dye Class (*One Letter Abbreviation*)	**Major Chemical Species**	**Anode Anchoring Moiety**	**HOMO/LUMO (eV)**
Anthocyanins (*A*)	Cyanidin-3-Glucoside [19]	OH	−5.89/−2.33 [47]
Betalins (*B*)	Betanin [20]	COOH	−4.75/−1.95 [48]
Curcuminoids (*K*)	Curcumin [21]	C=O, OH	−5.55/−1.97 [49]
Chlorophyll (*C*)	Chlorophyll a,b [22]	C=O	−5.93/−2.97 [50]
Xanthonoids (*M*)	*α*-Mangostin [23]	C=O, OH	−4.81/−2.27 [44]
Phycobilins (*P*)	Phycobilin [24]	COOH	−6.10/−3.85 [51]

References

1. Sharma, K.; Sharma, V.; Sharma, S. Dye-Sensitized Solar Cells: Fundamentals and Current Status. *Nanoscale Res. Lett.* **2018**, *13*, 1. [CrossRef] [PubMed]
2. O'Regan, B.; Grätzel, M. A low-cost, high-efficiency solar cell based on dye-sensitized colloidal TiO_2 films. *Nature* **1991**, *353*, 737–740. [CrossRef]
3. Grätzel, M. Conversion of sunlight to electric power by nanocrystalline dye-sensitized solar cells. *J. Photochem. Photobiol.* **2004**, *164*, 3–14. [CrossRef]
4. Calogero, G.; Bartolotta, A.; Di Marco, G.; Di Carlo, A.; Bonaccorso, F. Vegetable-Based Dye-Sensitized Solar Cells. *Chem. Soc. Rev.* **2015**, *44*, 3244–3294. [CrossRef] [PubMed]
5. Bhuiyan, M.; Fahmid, K.; Manir, M.; Rahaman, M.; Hossian, M.; Barua, P.; Ghosh, B.; Mitsugi, F.; Ikegami, T.; Huque, S.; et al. Effect of Combination of Natural Dyes and the Blocking Layer on the Performance of DSSC. In *Elseman, Solar Cells-Theory, Materials and Recent Advances*; IntechOpen: London, UK, 2021. [CrossRef]
6. Chang, H.; Kao, M.; Chen, T.; Chen, C.; Cho, K.; Lai, X. Characterization of Natural Dye Extracted from Wormwood and Purple Cabbage for Dye-Sensitized Solar Cells. *Int. J. Photoenergy* **2013**, *2013*, 159502. [CrossRef]
7. Cho, K.; Chang, H.; Chen, C.; Kao, M.; Lai, X. A Study of Mixed Vegetable Dyes with Different Extraction Concentrations for Use as a Sensitizer for Dye-Sensitized Solar Cells. *Int. J. Photoenergy* **2014**, *2014*, 492747. [CrossRef]
8. Golshan, M.; Osfouri, S.; Azin, R.; Jalali, T.; Moheimani, N. Co-sensitization of natural and low-cost dyes for efficient panchromatic light-harvesting using dye-sensitized solar cells. *J. Photochem. Photobiol. A Chem.* **2021**, *417*, 113345. [CrossRef]
9. Hosseinnezhad, M.; Gharanjig, K.; Moradian, S.; Reza-Saeb, M. In quest of power conversion efficiency in nature inspired dye-sensitized solar cells: Individual, co-sensitized or tandem configuration? *Energy* **2017**, *134*, 864–870. [CrossRef]
10. Kabir, F.; Bhuiyan, M.; Hossian, M.; Bashar, H.; Rahaman, M.; Manir, M.; Ullah, S.; Uddin, S.; Mollah, M.; Kahn, R.; et al. Improvement of efficiency of Dye Sensitized Solar Cells by optimizing the combination ratio of Natural Red and Yellow dyes. *Optik* **2019**, *179*, 252–258. [CrossRef]
11. Liu, B.; Zhao, X.; Luo, W. The synergistic effect of two photosynthetic pigments in dye-sensitized mesoporous TiO_2 solar cells. *Dye. Pigment.* **2008**, *76*, 327–331. [CrossRef]
12. Lo, Y.; Chang, H. Pomegranate leaves and mulberry fruit as natural sensitizers for dye-sensitized solar cells. *Sol. Energy* **2010**, *84*, 1833–1837. [CrossRef]
13. Obi, K.; Frolova, L.; Fuierer, P. Preparation and performance of prickly pear (*Opuntia phaeacantha*) and mulberry (*Morus rubra*) dye-sensitized solar cells. *Sol. Energy* **2020**, *208*, 312–320. [CrossRef]
14. Orona-Navar, A.; Aguilar-Hernández, I.; López-Luke, T.; Zarazúa, I.; Romero-Arellano, V.; Guerrero, J.P.; Ornelas-Soto, N. Photoconversion efficiency of Titania solar cells co-sensitized with natural pigments from cochineal, papaya peel and microalga Scenedesmus obliquus. *J. Photochem. Photobiol. A Chem.* **2020**, *388*, 112216. [CrossRef]
15. Patni, N.; Pillai, S.; Sharma, P. Effect of using betalain, anthocyanin and chlorophyll dyes together as a sensitizer on enhancing the efficiency of dye-sensitized solar cell. *Int. J. Res. Energy* **2020**, *44*, 10846–10859. [CrossRef]

16. Prabavathy, N.; Shalini, S.; Balasundaraprabhu, R.; Velauthapillai, D.; Prasanna, S.; Balaji, G.; Muthukumarasamy, N. Algal buffer layers for enhancing the efficiency of anthocyanins extracted from rose petals for natural dye-sensitized solar cell (DSSC). *Int. J. Energy Res.* **2017**, *42*, 790–801. [CrossRef]
17. Puspitasari, N.; Amalia, S.; Yudoyono, G. Effect of Mixing Dyes and Solvent in Electrolyte Toward Characterization of Dye Sensitized Solar Cell Using Natural Dyes as The Sensitizer. In *IOP Conference Series: Materials Science and Engineering*; IOP Publishing: Bristol, UK, 2017; Volume 214, p. 012022. [CrossRef]
18. Ramamoorthy, R.; Radha, N.; Maheswari, G.; Anandan, S.; Manoharan, S.; Williams, R. Betalain and anthocyanin dye-sensitized solar cells. *J. Appl. Electrochem.* **2016**, *46*, 929–941. [CrossRef]
19. Manz, N. Optimizing the Combination of Natural Pigments for Co-Sensitization of Panchromatic TiO_2 Dye Sensitized Solar Cells. Master's Thesis, New Mexico Institute of Mining and Technology, Socorro, NM, USA, April 2022.
20. Ahmadiani, N.; Robbins, R.; Collins, T.; Giusti, M. Anthocyanins Contents, Profiles, and Color Characteristics of Red Cabbage Extracts from Different Cultivars and Maturity Stages. *Agric. Food Chem.* **2014**, *62*, 7524–7531. [CrossRef]
21. Gouvêa, A.; Santiago, M.; Schultz, D.; Pacheco, S.; Godoy, R.; Cabral, L. Anthocyanins standards (cyanidin-3-O-glucoside and cyanidin-3-O-rutinoside) isolation from freeze-dried açaí (Euterpe oleraceae Mart.) by HPLC. *Food Sci. Technol.* **2012**, *32*, 43–46. [CrossRef]
22. Khatabi, O.; Hanine, H.; Elothmani, D.; Hasib, A. Extraction and determination of polyphenols and betalain pigments in the Moroccan Prickly pear fruits (*Opuntia ficus indica*). *Arab. J. Chem.* **2016**, *9*, 278–281. [CrossRef]
23. Tayyem, R.; Heath, D.; Al-Delaimy, W.; Rock, C. Curcumin Content of Turmeric and Curry Powders. *Nutr. Cancer* **2006**, *55*, 126–131. [CrossRef] [PubMed]
24. Priyadarsini, K. The Chemistry of Curcumin: From Extraction to Therapeutic Agent. *Molecules* **2014**, *19*, 20091–20112. [CrossRef]
25. Bohn, T.; Walczyk, T.; Leisibach, S.; Hurrell, R. Chlorophyll-bound Magnesium in Commonly Consumed Vegetables and Fruits: Relevance to Magnesium Nutrition. *J. Food Sci.* **2006**, *69*, 347–350. [CrossRef]
26. Li, Y.; Scales, N.; Blankenhip, R.; Willows, R.; Chen, M. Extinction coefficient for red-shifted chlorophylls: Chlorophyll d and chlorophyll f. *Biochim. Biophys. Acta* **2012**, *1817*, 1292–1298. [CrossRef] [PubMed]
27. Tsai, S.; Chung, P.; Owaga, E.; Tsai, I.; Wang, P.; Tsai, J.; Yeh, T.; Hsieh, R. Alpha-mangostin and mangsteen (*Garcinia mangostana Linn.*) pericarp extract reduces high fat-diet induced hepatic steatosis in rats by regulating mitochondria function and apoptosis. *Nutr. Metab.* **2016**, *13*, 133–152. [CrossRef] [PubMed]
28. Muchtaridi, M.; Suryani, D.; Qosim, W.; Saptarini, N. Quantitative analysis of a-Mangostin in Mangonsteen (*Garcinia mangostana* L.) pericarp extract from four district of west Java by HPLC method. *Int. J. Pharm. Pharm. Sci.* **2016**, *8*, 232–236.
29. Khandual, S.; Sanchez, E.; Andrews, H.; De-la-Rosa, J. Phycocyanin content and nutritional profile of Arthrospira platensis from Mexico: Efficient extraction process and stability evaluation of phycocyanin. *BMC Chem.* **2021**, *15*, 24. [CrossRef] [PubMed]
30. National Center for Biotechnology Information. PubChem Compound Summary for CID 197081, Cyanidin 3-O-Glucoside. Available online: https://pubchem.ncbi.nlm.nih.gov/compound/Cyanidin-3-O-glucoside (accessed on 10 February 2023).
31. National Center for Biotechnology Information. PubChem Compound Summary for CID 6540685, Betanine. Available online: https://pubchem.ncbi.nlm.nih.gov/compound/Betanine (accessed on 10 February 2023).
32. National Center for Biotechnology Information. PubChem Compound Summary for CID 969516, Curcumin. Available online: https://pubchem.ncbi.nlm.nih.gov/compound/Curcumin (accessed on 10 February 2023).
33. National Center for Biotechnology Information. PubChem Compound Summary for CID 12085802, Chlorophyll a. Available online: https://pubchem.ncbi.nlm.nih.gov/compound/12085802 (accessed on 10 February 2023).
34. National Center for Biotechnology Information. PubChem Compound Summary for CID 5281650, Alpha-Mangostin. Available online: https://pubchem.ncbi.nlm.nih.gov/compound/alpha-Mangostin (accessed on 10 February 2023).
35. National Center for Biotechnology Information. PubChem Compound Summary for CID 6438349, Phycobilin. Available online: https://pubchem.ncbi.nlm.nih.gov/compound/Phycobilin (accessed on 10 February 2023).
36. Bett, J.; Radial Basis Function USRA. Github Repository. October 2016. Available online: https://github.com/jessebett/Radial-Basis-Function-USRA (accessed on 1 December 2022).
37. Guo, M.; Xie, K.; Lin, J.; Yong, Z.; Tung-Yip, C.; Zhou, L.; Wang, Y.; Huang, H. Design and coupling of multifunctional TiO_2 nanotube photonic crystal to nanocrystalline titania layer as semi-transparent photoanode for dye-sensitized solar cell: Supplementary information. *Energy Environ. Sci.* **2012**, *12*, 9881–9888. [CrossRef]
38. Manz, N.; Bauman, A.; Brudos, E. Optimizing the Combination of Natural Pigments for Co-Sensitization of Panchromatic TiO_2 Dye Sensitized Solar Cells [dataset]. *Mendeley Data* **2022**, V3. [CrossRef]
39. Pitigala, P.; Henary, M.; Perera, A. Effects of Physical Orientation of Dye Molecules and Molecular Orbitals on Performance of Solid-State Dye Sensitized Solar Cells. *Mater. Today Proc.* **2020**, *23*, 43–48. [CrossRef]
40. Sewvandi, G.; Kakimoto, M.; Chen, C.; Hu, D.; Abeygunawardhana, P.; Feng, Q. Controlling Dye Coverage Instead of Addition of Organic Acid to Reduce Dye Aggregation in Dye-Sensitized Solar Cells. *Sol. Energy* **2020**, *202*, 507–513. [CrossRef]
41. National Renewable Energy Laboratory (NREL). Reference Air Mass 1.5 Spectra. Available online: https://www.nrel.gov/grid/solar-resource/spectra-am1.5.html (accessed on 1 December 2022).
42. Matsuzaki, H.; Murakami, T.; Masaki, N.; Furube, A.; Kimura, M.; Mori, S. Dye Aggregation Effect on Interfacial Electron-Transfer Dynamics in Zinc Phthalocyanine-Sensitized Solar Cells. *J. Phys. Chem.* **2014**, *118*, 17205–17212. [CrossRef]

43. Cisneros, R.; Beley, M.; Lapicque, F. A study of the impact of co-adsorbents on DSSC electron transfer processes: Anti-pi-stacking vs. shield effect. *Phys. Chem. Chem. Phys.* **2016**, *18*, 9645–9651. [CrossRef] [PubMed]
44. Ismail, M.; Ludin, N.; Hamid, N.; Ibrahim, M.; Sopain, K. The Effect of Chenodeoxycholic Acid (CDCA) in Mangosteen (Garcinia mangostana) Pericarps Sensitizer for Dye-Sensitized Solar Cell (DSSC). *J. Phys. Conf. Ser.* **2018**, *1083*, 012018. [CrossRef]
45. Zaffino, C.; Russo, B.; Bruni, S. Surface-enhanced Raman scattering (SERS) study of Anthocyanidins. *Mol. Biomol. Spectrosc.* **2015**, *149*, 41–47. [CrossRef] [PubMed]
46. Nakano, S.; Sugimoto, N. The structural stability and catalytic activity of DNA and RNA oligonucleotides in the presence of organic solvents. *Biophys. Rev.* **2016**, *8*, 11–23. [CrossRef] [PubMed]
47. Yuliarto, B.; Prima, E.; Dipojono, H. Theoretical Investigation of Anthocyanidin Algycones as Photosensitizers for Dye-Sensitized TiO_2 Solar Cells. In *Advanced Materials Research*; Trans Tech Publications Ltd.: Bäch, Switzerland, 2015. [CrossRef]
48. Ranjitha, S.; Aroulmoji, V.; Dhevi, R.L.; Rajarajan, G.; Gnanendra, S. Priminence of Using Betalin and Cubebin as Natural Dye Sensitizers for the Design of Eco-Friendly DSSC's. *Int. J. Adv. Sci. Eng.* **2018**, *4*, 726. [CrossRef]
49. Shahab, S.; Azarakhski, F.; Sheikhi, M. DFT Study of Physiorption Effect of the Curcumin on CNT(8,0-6) Nanotube for Biological Applications. *Chin. J. Struct. Chem.* **2019**, *38*, 42–57. [CrossRef]
50. De Lile, J.R.; Kang, S.G.; Son, Y.A.; Lee, S.G. Do HOMO-LUMO Energy Levels and Band Gaps Provide Sufficient Understanding of Dye-Sensitizer Activity Trends for Water Purification? *ACS Omega* **2020**, *5*, 15052–15062. [CrossRef] [PubMed]
51. Mishima, K.; Shoji, M.; Umena, Y.; Boero, M.; Shigeta, Y. Role of the Propinoic Acid Side Chain of C-Phycocyanin Chromophores in the Excited States of the Photosynthesis Process. *Bull. Chem. Soc. Jpn.* **2020**, *93*, 1509–1519. [CrossRef]